Title

Carbon nanotube thin film strain sensor models assembled using nano- and micro-scale imaging

Journal

Computational Mechanics, 60(1)

ISSN

0178-7675

Authors

Lee, Bo Mi
Loh, Kenneth J
Yang, Yuan-Sen

Publication Date

2017-07-01

DOI

10.1007/s00466-017-1391-6

Peer reviewed

Carbon Nanotube Thin Film Strain Sensor Models Assembled using Nano- and Micro-Scale Imaging

Bo Mi Lee[1] · Kenneth J. Loh[1,*] · Yuan-Sen Yang[2]

[1] Department of Structural Engineering, University of California-San Diego, La Jolla, CA 92093-0085, USA
[2] Department of Civil Engineering, National Taipei University of Technology, Taipei 10608, Taiwan

[*]Corresponding author and contact information:
E-mail: kenloh@ucsd.edu
Phone: +1 858-822-0431
Fax: +1 858-534-1310

Abstract Nanomaterial-based thin films, particularly those based on carbon nanotubes (CNT), have brought forth tremendous opportunities for designing next-generation strain sensors. However, their strain sensing properties can vary depending on fabrication method, post-processing treatment, and types of CNTs and polymers employed. The objective of this study was to derive a CNT-based thin film strain sensor model using inputs from nano-/micro-scale experimental measurements of nanotube physical properties. This study began with fabricating ultra-low-concentration CNT-polymer thin films, followed by imaging them using atomic force microscopy. Image processing was employed for characterizing CNT dispersed shapes, lengths, and other physical attributes, and results were used for building five different types of thin film percolation-based models. Numerical simulations were conducted to assess how the morphology of dispersed CNTs in its 2D matrix affected bulk film electrical and electromechanical (strain sensing) properties. The simulation results showed that CNT morphology had a significant impact on strain sensing performance.

Keywords: atomic force microscopy; carbon nanotube; nanocomposite; percolation model; strain sensor; structural health monitoring; thin film.

1 Introduction

Engineered structures (*i.e.*, aerospace, civil, marine, and mechanical systems, among others) are constantly subjected to complex loads (*i.e.*, live loads, fatigue, impact, and environmental deterioration) throughout their service lifetime. A direct result is the formation of defects, flaws, or damage precursors that begin at the microscopic material level, which can eventually propagate to cause component or catastrophic structural failure if left undetected over time [1]. Conventional means of monitoring the health of these structures rely on visual inspection, but not only is this process labor intensive, expensive, time consuming, and possibly subjective, detecting subsurface or minute damage is also challenging.

A viable alternative is to measure structural strains, which is typically performed using foil-based strain gages. Given structural component material properties, one can then use strain measurements for inferring stresses and to assess the possibility of potential failure. However, one of the main limitations of strain gages is that they are inherently discrete transducers. Strain measurements are only obtained at instrumented sensor locations. Typical installations in practical applications require a dense network of sensors installed, along with corresponding coaxial wires for power supply and data transfer. These factors drive up monitoring system costs, and the impracticality of instrumenting a very dense sensor network limits their effectiveness for detecting the severities and locations of damage features.

Recently, a new sensing paradigm that employs nanocomposite coatings or thin films deposited onto or embedded in structural components has emerged. The innovation is that these materials-based sensors are designed with electrical properties that are sensitive to external stimuli (*e.g.*, mechanical, chemical, and thermal parameters) at every location of the material. In principle, one could then measure the sensor's electrical response at every location to obtain sensed information across the entire spatial domain.

To date, a variety of different nanomaterials have been employed for designing nanocomposite thin film sensors, such as by using carbon black (CB) [2], carbon nanotubes [3], graphene [4], and nanoparticles [5]. Knite *et al.* [2] demonstrated that the electrical resistance of CB-polyisoprene changed when subjected to uniaxial loading. Bae *et al.* [4] used photolithography to build transparent graphene-based thin films, which was then attached onto a polydimethylsiloxane (PDMS) substrate. Strain sensing tests revealed that its electrical resistance increased linearly at relatively low levels of applied strain ($\varepsilon <$ 18,000 $\mu\varepsilon$) and increased nonlinearly at higher strains (18,000 $\mu\varepsilon < \varepsilon <$ 71,000 $\mu\varepsilon$). On the other hand, Maia *et al.* [6] developed mesoporous silica nanomaterial-based corrosion-sensitive coatings. The corrosion sensitive coatings were fabricated by loading mesoporous silica nanocontainers (Si-NC) with phenolphthalein (PhPh) embedded in transparent epoxy. It was demonstrated that when aluminum and magnesium alloy substrates coated with the sensing material were exposed to alkaline environments, PhPh was released from Si-NC to reveal a pink color, indicating the occurrence of corrosion.

Among the wide variety of nanomaterials, carbon nanotubes (CNT) [7] have gained significant attention due to their impressive electrical, mechanical, and electromechanical properties [8], which stem from their unique nano-structure (*i.e.*, high aspect ratio and carbon-carbon covalent bond structure). For instance, Stampfer *et al.* [9] quantified the electromechanical properties of a 600 nm-long single-walled carbon nanotube (SWCNT) by suspending it underneath a 200 nm-wide gold (Au) cantilever. Then, an atomic force microscope (AFM) was used to apply force to the Au cantilever to induce tensile strains in the SWCNT. It was shown that the maximum strain sensitivity of SWCNT was 2,900, which confirmed its potential for strain sensing.

Following the same design philosophy, CNTs have been incorporated in polymer matrices so as to realize nanocomposite sensors whose electrical properties are sensitive to mechanical deformations or strains. Early work by Dharap *et al.* [10] fabricated SWCNT buckypapers using a vacuum filtration process, and the buckypaper exhibited a linear change in voltage due to applied tensile and compressive strains to $\pm$400 $\mu\varepsilon$. Pham *et al.* [11] assembled multi-walled carbon nanotube (MWCNT)-poly(methyl methacrylate) (PMMA) films using a solution casting method and showed that its electromechanical properties varied with applied tensile cyclic strains to 10,000 $\mu\varepsilon$. Loyola *et al.* [12] assembled, using a layer-by-layer method, MWCNT-polyelectrolyte thin films and deposited them onto glass-fiber-fabrics for measuring strains in fiber-reinforced polymer (FRP) composites. Time-domain resistance and frequency-domain electrical impedance spectroscopy (EIS) were used to characterize their strain sensing performance. Instead of depositing CNT-polymer films onto structural surfaces, Gupta *et al.* [13] proposed self-sensing concrete by spray-coating pristine aggregate surfaces with MWCNT-latex thin films prior to their use for casting mortar and concrete. In addition to showing that resistance changes due to applied strains or damage, an electrical impedance tomography (EIT) algorithm that could reconstruct the self-sensing concrete's spatial distribution of electrical properties was implemented for achieving spatial sensing. The severity and location of damage (induced by drilling holes) was successfully detected.

Besides experimental investigations of CNT-based strain sensors, computational models have also been developed for explaining the underlying mechanisms that enable piezoresistivity. Early work began with simulating the electrical properties of CNT-based nanocomposites. For example, Behnam *et al.* [14] simulated a 2D nanotube-network model and demonstrated how nanotube parameters (*e.g.*, tube-tube contact resistance to nanotube resistance ratio, nanotube length, density, and alignment) affected the resistivity of the model. Bao *et al.* [15] incorporated the Landauer-Büttiker formula in a 3D mathematical model to consider both tunneling and direct contact resistances. The electrical conductivities of the model with different nanotube volume fractions were simulated. The results showed that the model conductivity increased with higher inclusions of CNTs. On the other hand, Hu *et al.* [16] applied uniaxial strains to a 3D CNT-based nanocomposite model. Tunneling was regarded as the dominant mechanism that determined electromechanical behavior, and the change in resistance of individual CNTs when strained was excluded. It was shown that the model became less sensitive to strains with higher CNT concentrations, similar to what Rahman *et al.* [17] found. More recently, Lee *et al.* [18] formulated a 2D percolation-based CNT-network model that characterized the effects of CNT parameters (*i.e.*, CNT length and density) on the electrical and electromechanical properties of the nanocomposite. A particular focus was to study how CNTs with different intrinsic strain sensitivities affected bulk film strain sensitivity. While higher intrinsic strain sensitivities of the CNTs translated to the large-scale, a decrease in bulk strain sensitivity was observed as CNT density in the film was increased. This trend was consistent with other experimental findings [11, 19], but other researchers [3, 20] discovered the opposite too.

Despite these advances, studies that provide direct linkages between experimental investigations and numerical simulations of CNT-based thin film strain sensors are limited [16, 21]. In these studies, the morphological features of CNT-based nanocomposites were somewhat simplified during modeling [16-18], where most studies assumed that CNTs were straight and of uniform length, both of which are rarely true in actual nanocomposites. In fact, experimental studies [3, 22] revealed that nanocomposites fabricated using different types of CNTs resulted in different electromechanical characteristics. For example, Loh *et al.* [3] found that unpurified CNTs exhibited poor piezoresistivity, whereas purified nanotubes performed much better. On the other hand, Yin *et al.* [22] showed that different types of MWCNTs embedded in epoxy can lead to both linear and nonlinear electromechanical behavior.

Therefore, the objective of this study was to derive a 2D CNT-based thin film model that could adequately describe the electrical and electromechanical properties of a specific type of CNT-based nanocomposite thin film. Instead of assuming CNT morphology and their physical properties, their as-dispersed and deposited shapes, as well as statistical distributions of CNT lengths, were obtained from direct experimental measurements and then incorporated in the percolation-based model. This study started with the fabrication of ultra-low-concentration MWCNT-PSS thin films. Then, AFM images of MWCNT-PSS thin films were obtained to resolve the individual nanotubes deposited. Image analysis and processing were employed to characterize CNT length distributions and their preferential deposited geometric shapes. These results were incorporated in the 2D numerical model, and their electrical and strain sensing properties were subsequently computed and evaluated.

2 Carbon nanotube characterization

2.1 Materials

MWCNTs were purchased from SouthWest NanoTechnologies with a reported median outer diameter of 10 nm, median length of 3.0 μm, and purity >99%. Poly(sodium 4-styrenesulfonate) (PSS) ($M_W \approx$ 1,000,000) was acquired from Sigma-Aldrich.

2.2 AFM sample preparation

MWCNT-PSS thin films were prepared for AFM characterization so as to investigate the morphology and physical characteristics of dispersed and as-deposited MWCNTs. MWCNT-PSS thin film assembly started with the preparation of 1 *wt.*% PSS aqueous solution. PSS powder was dissolved in deionized (DI) water by 60 min of bath ultrasonication (135 W, 42 kHz). Then, 1 mg/mL of MWCNTs was dispersed in 1 *wt.*% PSS solution. Uniform dispersion was achieved by subjecting the MWCNT-PSS mixture to 180 min of bath ultrasonication and 60 min of high-energy probe sonication (3 mm tip, 150 W, 22 kHz) [3]. The 1 mg/mL MWCNT-PSS solution was diluted with DI water to create ultra-low-concentration MWCNT-PSS solutions (*i.e.*, 1 μg/mL). The rationale for preparing 1 μg/mL MWCNT-PSS solutions was so that AFM imaging could resolve the physical properties of individual nanotubes as opposed to imaging a percolated network (which would then be difficult to characterize the properties of individual nanotubes).

The 1 μg/mL MWCNT-PSS dispersion was then used as is for preparing thin film samples for AFM imaging. Here, a silicon substrate was used. Prior to

film deposition, silicon wafers were treated with piranha solution (H_2SO_4:H_2O_2 = 17:9) for 30 min to remove organic residues on the wafer surface and to enhance hydrophilicity. The cleaned silicon wafer was cleaved to obtain smaller chips (~7×7 mm^2) using a diamond scribe. A small drop of diluted MWCNT-PSS solution was pipetted onto the substrate and left to air-dry in a fume hood for 12 h to form the final ultra-low-concentration thin film (Fig. 1).

2.3 Image analysis procedure

To date, many researchers have sought to take advantage of micro- or nano-scale images obtained by scanning electron microscopy (SEM), transmission electron microscopy (TEM), and AFM to characterize CNT-based thin films. For example, Dharap *et al.* [10] and Loh *et al.* [3] employed SEM for investigating the quality of nanotube dispersion in thin films. The CNTs' physical properties (*i.e.*, nanotube length and diameter) can then be estimated from these SEM images, but the challenge is that they form complex 3D networks, and it is often difficult to identify the start- and end-points of individual nanotubes. Gommes *et al.* [23] used TEM images of MWCNTs to measure their inner and outer radii. It was shown that annealing at 2,500 °C decreased MWCNT lengths. Tenent *et al.* [24] dispersed SWCNTs in a sodium carboxymethyl cellulose (CMC) aqueous solution and varied sonication times (*i.e.*, 10 and 60 min). Diluted SWCNT-CMC solution was spin-coated to form SWCNT-CMC thin films on silicon. Then, the lengths of 300 SWCNTs in the thin films were measured using AFM and Gwyddion software. The results showed that SWCNTs subjected to 60 min of sonication (which yielded a mean length of 0.55 μm) were significantly shorter than those treated with 10 min of sonication (where mean SWCNT length was 1.32 μm). Instead of focusing on individual CNTs, Timmermans *et al.* [25] characterized the morphology of SWCNT-networks fabricated using four different techniques, namely electrostatic precipitation, thermal precipitation, press transfer from a filter, and dissolving the filter. The SEM images clearly showed different morphological features of SWCNT-networks depending on the particular fabrication method employed.

As mentioned before, a primary focus of this work was not just to assume the physical parameters and dispersed shapes of CNTs when generating the numerical model but, instead, to integrate actual experimental measurements of nanotube properties (*i.e.*, dispersed shapes of CNTs and their lengths) with appropriate uncertainty quantification (*i.e.*, CNT length distribution). In this study, an Asylum MFP-3D AFM was employed to analyze the surface topography of MWCNT-PSS thin films deposited on silicon substrates. AFM was performed in tapping mode using a silicon cantilever (FMV-A, Bruker) with aluminum coating on the back and a spring constant of ~1.80 N/m. AFM imaging was initially conducted using a coarse scan size of 20 μm, and then the location of the target MWCNT was set as the next scan position to capture 5×5 μm^2 images.

Some representative AFM images are shown in Fig. 2. Both amplitude (Fig. 2a) and height images (Figs. 2b-e) clearly showed that MWCNTs were embedded in the PSS matrix. As mentioned earlier, the specimen was assembled in a manner to deposit individual MWCNTs (*i.e.*, non-percolated) with very low concentrations of PSS. The drying process does not form a continuous thin film but rather localized regions with individual MWCNTs deposited on the silicon wafer. Since AFM imaging was performed on individual MWCNTs, the heights reported Figs. 2b-e sufficiently characterized the physical properties of MWCNTs, as opposed to the PSS matrix. In addition, AFM imaging revealed the presence of ultra-short MWCNTs (*i.e.*, of a few nanometers). These MWCNTs were thought to be cut during high-energy tip sonication [24]; these were ignored during the characterization process, since they were unlikely to help form a percolated network even when high concentrations of nanotubes are used for thin film fabrication. One particular important finding here is that, unlike many CNT-based numerical models that assumed CNTs to be straight [16-18], the AFM images revealed a variety of shapes when they are deposited experimentally.

2.4 Image analysis results

MWCNT length measurements were obtained from AFM height images. The images were processed and analyzed using *ImageJ,* an image processing software. The image analysis procedure and intermediate steps are illustrated in Fig. 3. First, an AFM image (RGB image) was imported to *ImageJ*. The correct scale of the image was defined using the scale bar in the AFM image. Then, a region of interest in which an MWCNT was located was selected (Fig. 3a). Second, the RGB image was converted into a gray-scale image (8-bit). Then, the resulting gray-scale image shown in Fig. 3(b) was enhanced by applying built-in commands (*i.e.*, sharpening, smoothing, median filter, and fast Fourier transform filter, among others) and converted into a binary black and white image (Fig. 3c). Finally, the edges that sum to obtain each MWCNT's perimeter were identified and measured. Since the aspect ratio of each MWCNT is high, its length was estimated as half of the total perimeter (*i.e.*, the diameter of the MWCNT was assumed to be negligible).

To verify *ImageJ* length estimation, an MWCNT length was measured using a customized *MATLAB* program and then compared as follows. Similar to *ImageJ* analysis, an AFM image (RGB) was imported into *MATLAB* and converted into gray-scale. A target MWCNT was identified and divided into linear segments. The "measure distance" tool was used to measure the pixel distance of each linear segment in the image. Using the tool, the distance of the scale bar was measured for calibration. The measured segments were then added and converted to its physical length (in μm) using the ratio of the real distance of scale bar to pixel distance. The results are summarized in Table 1. It can be seen that the measured length using this linear segment method was comparable to that obtained from *ImageJ* (*i.e.*, herein referred to as the perimeter method). However, the length measured by the linear segment method was smaller than the perimeter method. One possible reason can be the fact that the perimeter method did not exclude the diameter of MWCNTs. In addition, results from linear segment estimation depend on the number of segments used for characterizing each MWCNT, where estimated length would increase with more linear segments used (*i.e.*, due to the fact that the MWCNT is curved). Overall, the perimeter method with *ImageJ* was successfully validated and was used for the remainder of this study.

In total, the lengths of 20 MWCNTs were measured, which yielded an average length of 1.904 μm and a standard deviation of 0.506 μm. Fig. 4 shows the distribution of MWCNT lengths. In addition, a Gaussian distribution was fitted to the raw data, and one can find that fitting was adequate. It should be noted that the mean MWCNT length measured by image analysis was shorter than that reported by the manufacturer, which is 3 μm. A possible reason for this discrepancy is that MWCNTs were cut and shortened during sonication, as was reported in other studies [24].

3 Numerical modeling

3.1 Percolation-based model

A bottom-up approach was employed for building 2D CNT-based thin film numerical models. This work builds on the foundation established in a previous study [18], in which 2D percolation-based models were derived assuming that 3 μm-long CNTs represented straight, linear segments. Here, the uncertainties of as-deposited MWCNT lengths (*i.e.*, mean and standard deviation of MWCNT lengths) were incorporated when defining the numerical model. In addition, the model proposed herein also accounts for the different shapes of dispersed MWCNTs.

The 2D percolation-based thin film model was generated in *MATLAB* and followed a similar procedure reported in [18]. First, nanotube density (the number of CNTs or N) and the dimensions of the film (*i.e.*, length, L, and width, W) were defined. This work defined film size as 60×10 μm^2, and this geometry or aspect ratio was selected so as to be consistent with actual specimen aspect ratios that were experimentally tested [18]. Second, using the results from Section 2.4, the model assumed that CNT lengths (L_{CNT}) followed a Gaussian distribution identical to that obtained from image analysis, where the lengths of N CNTs were then generated using the "normrnd" function in *MATLAB*. Third, with each CNT length generated, CNTs of various shapes were randomly dispersed and deposited in the model space. Since AFM imaging of MWCNT-PSS thin films revealed that nanotubes can possess a wide variety of shapes, such as being nearly straight (Fig. 2b), kinked (Fig. 2c), and rounded (Fig. 2d), this work assumed three predominant shapes during modeling, as is shown in Fig. 5. The three different CNT shapes are: straight (CNT 1); two linear segments to form a kink with three nodes (CNT 2); and three linear segments with four nodes to form a rounded or a sinusoidal geometry (CNT 3). For simplicity, each linear segment was assumed to possess the same length. For example, CNT 2 and CNT 3 each had a segment length of $L_{CNT}/2$ and $L_{CNT}/3$, respectively. In addition, the angle at each node and between adjacent segments were randomly generated to be between 0° and 179°; here, 179° was used as the upper-limit to prevent overlap of segments in the same CNT, and this was consistent with observations from AFM imaging.

To randomly locate CNTs in the 2D model space, the first end-point of a CNT, (x_1, y_1), was generated using *MATLAB*'s random number generator and positioned to be within the film dimensions. The positions of other nodes (i) were determined using the segment length and angles (θ_{i-1}):

$$x_i = x_{i-1} + \frac{L_{CNT}}{i-1}\cos(\theta_{i-1}) \tag{1}$$

$$y_i = y_{i-1} + \frac{L_{CNT}}{i-1}\sin(\theta_{i-1}) \tag{2}$$

where i is the nodal number (ranges from 1 to 4 depending on the type of CNT defined). Periodic boundary conditions were implemented so that the model always contained the predefined number or density of CNTs.

In total, five different models were generated to investigate how the morphology of the dispersed CNT-network affected bulk film electrical and strain sensing properties. The first model (Model #1), which was the control case, included only 1D straight CNTs (CNT 1). The second, or Model #2, consisted of only CNTs with

two segments (CNT 2). Model #3 included only CNTs with three segments (CNT 3). Then, Model #4 and Model #5 were composed of different types of CNTs; Model #4 was composed of CNT 1 and CNT 2, while Model #5 consisted of all three different CNTs (CNT 1, 2, and 3). A representative Model #5 with N = 1,400 is shown in Fig. 5.

3.2 Electrical and electromechanical properties

Upon generating the five different thin film models, their electrical properties (*i.e.*, resistance) were simulated and characterized. First, the locations of CNT-to-CNT intersections (*i.e.*, junctions) were stored in a junction matrix. Once junction locations were found, the resistance of each CNT was calculated by considering each CNT as a resistive element [26]:

$$R_{CNT} = R_i + R_{Ohmic} + R_{jct} \tag{3}$$

where R_i is the theoretical intrinsic resistance of an SWCNT with perfect contact (6.5 kΩ), R_{Ohmic} is the Ohmic resistance caused by imperfect contact, and R_{jct} is the junction resistance. It should be mentioned that Ohmic resistance depends on junction-to-junction length. Junction resistance (R_{jct}) depends on the electrical properties of SWCNTs (*i.e.*, metallic or semiconducting depending on its chirality [27]) that comprise the junction. This study assumed that all CNTs were metallic to be consistent with the use of MWCNTs in the aforementioned experiments, and only metallic-metallic junctions of 98 kΩ existed [28]. It should be mentioned that, although the experimental tests were performed using MWCNTs, the numerical model does not differentiate between SWCNTs and MWCNTs, nor does it consider nanotube diameters for the purpose of simplifying the model [29].

Then, each nanotube's resistance was incorporated to determine the resistance of the entire CNT-network by formulating a conductance matrix for analyzing the thin film's electrical properties. The reciprocal of CNT resistance, which is conductance, was used to construct the conductance matrix, [G]:

$$[G] = \begin{bmatrix} g_{11} & \cdots & g_{1i} & \cdots & g_{1n} \\ \vdots & \ddots & & & \vdots \\ g_{i1} & & g_{ii} & & g_{in} \\ \vdots & & & \ddots & \vdots \\ g_{n1} & \cdots & g_{ni} & \cdots & g_{nn} \end{bmatrix} \tag{4}$$

where the diagonals (g_{ii}) are the summation of the conductance values connected to junction i, and the non-diagonal terms (g_{ij}) are the negative of the summation of the conductance values between junctions i and j. [G] is a square matrix of order n, which is equal to the total number of junctions. It should be noted that a straight CNT-network can have only one conducting component between two junctions (i and j). On the other hand, other CNT-networks can have more than one conducting component between two junctions. Then, for the models investigated in this study, it was assumed that the electrodes were located on the top and bottom edges of the thin film model. A potential difference of 10 V was applied across the electrodes to excite the system. Using [G] and the applied voltage, Kirchhoff's current law and the conductance version of Ohm's law were then used to determine the resistance of the entire CNT-network. More details can be found in Lee *et al.* [18]. Given that the dimensions of all the models were kept the same, resistance is comparable to resistivity.

In addition, deformations were also applied to the thin film model for evaluating its electromechanical or strain sensing properties. To be specific, uniaxial tensile and compressive strains to ±0.01 (in 0.0025 increments) were applied to the model, and the electrical properties at each strain state were calculated. The model was assumed to be homogeneous and isotropic, and strain was applied uniformly to the entire film. This assumption greatly simplified computations by neglecting the CNT-matrix interfaces, especially since it has been shown from finite element models that stress concentrations would exist at the terminating ends of each tube [30]. Regardless, the coordinates of each strained CNT were then updated. The electrical resistance of the strained CNT-network was subsequently calculated following the aforementioned procedure. It should be noted that an intrinsic strain sensitivity for metallic nanotubes (S_{CNT} = 60) was incorporated in the model [31].

4 Results and discussion

4.1 Nominal electrical properties

CNT thin film percolation-based models were formulated according to the steps discussed in Section 3, and the nominal or unstrained electrical resistance of five different models were calculated. However, before characterizing the nominal electrical properties of the CNT-network model, each model's percolation threshold was evaluated. The thin film model's percolation threshold is defined as the number of nanotubes required in which the percolation probability reached ~50% [32]. Therefore, the percolation thresholds for Models #1, #2, #3, #4, and #5 were identified as N = 1,140, 1,325, 1,440, 1,230, and 1,322, respectively.

The percolation threshold was used as the minimum number of nanotubes needed to obtain a percolated system so that electrical current could propagate

through the film, so that the model's electrical resistance could be computed. Therefore, for this study, the mininum CNT density used was N = 1,400, and density was varied for N = 1,400, 1,800, and 2,400. CNT density was altered so as to model the incorporation of different carbon nanotube weight fractions or concentrations in the films. The results are summarized in Fig. 6. Here, 20 simulations were conducted for each CNT concentration. It can be observed that all five models showed a decrease in electrical resistance with higher CNT densities, which is consistent with percolation theory.

Although all models possessed identical CNT length distributions (*i.e.*, same average CNT length and standard deviation of CNT lengths), the different sets of models were constructed using different CNT shapes, which caused the models to exhibit different nominal electrical resistances. In particular, the model that used CNTs represented by three linear segments (Model #3) exhibited the highest electrical resistance (lowest conductance), whereas the model with only straight CNTs (Model #1) had the lowest electrical resistance. This result directly supports the hypothesis that CNT geometry affects bulk film electrical properties.

Despite these differences, within each of the five model cases, electrical resistance decreased as the density of CNTs increased. These results were consistent with other experimental and numerical investigations [22, 33, 34]. For example, as mentioned in Section 1, Yin *et al.* [22] utilized two different types of MWCNTs to fabricate two different epoxy-based nanocomposites. SEM images revealed that one type of MWCNTs dispersed in the epoxy matrix were significantly curved as compared to the other sample set. The result was that films consisting of curved nanotubes yielded a bulk film conductivity of 0.00192 S/m, which is significantly lower than the other case (65.8 S/m) with mostly straight nanotubes (*i.e.*, the system with straight nanotubes yielded higher electrical conductivity or lower resistance, which is consistent with the findings presented in this work). Similarly, Li *et al.* [33] generated 2D CNT-based nanocomposite models that considered two different CNT shapes (*i.e.*, straight and curved). It was shown that the model with curved CNTs exhibited lower conductivity versus the other with only straight CNTs. A curl ratio was defined as the ratio between the CNT length to effective CNT length (*i.e.*, maximum distance between two arbitrary points of a CNT). The results showed the model's electrical conductivity would decrease with higher CNT curl ratios, which is also consistent with the findings presented here.

In this study, a similar effective CNT length was defined [33]. In each thin film model, effective lengths of N CNTs were calculated and averaged. Then, the model's electrical resistance was plotted with respect to effective CNT length, as shown in Fig. 7. For all N cases, Model #3 had a shorter effective length than the other four models, while Model #1 yielded the longest effective length. In addition, the results showed that effective length was not affected by CNT density. For example, the effective length of Model #3 was 1.484, 1.488, and 1.486 μm for N = 1,400, 1,800, and 2,400, respectively. On the other hand, when the number of CNTs was kept the same, the model with shorter effective lengths showed higher resistances. These results confirmed that bulk film electrical properties were sensitive to effective CNT lengths.

4.2 Strain sensing properties

The electromechanical or strain sensing properties of the CNT-based thin film models were also investigated. As mentioned earlier in Section 3.2, the resistance of the film at the various strain states were calculated. Fig. 8 plots the normalized change in resistance (R_{norm}) of five representative thin film models as a function of applied strains, when N = 1,400.

$$R_{norm} = \frac{\Delta R}{R_i} \tag{5}$$

where R_i is the nominal or initial unstrained resistance, and ΔR is the change in resistance between the bulk film resistance of the model at a certain strain state with respect to its unstrained baseline (or nominal) resistance.

First, all five models exhibited an increase in film resistance in tandem with increasingly applied strains. Second, it can be observed that R_{norm} of all five models exhibited a linear relationship with respect to applied strain. On the other hand, the values of R_{norm} at the same strain state varied depending on different thin film models. For instance, when applied strain was 0.01, the model based on only straight CNTs (Model #1) had a larger R_{norm} value (1.145×10^{-2}) than the other four cases (1.051×10^{-2}, 0.970×10^{-2}, 1.076×10^{-2}, and 1.048×10^{-2} for Models #2, #3, #4, and #5, respectively).

To better quantify its strain sensing behavior, strain sensitivity (S) or gage factor of the bulk film was evaluated as follows:

$$S = \frac{R_{norm}}{\Delta\varepsilon} \tag{6}$$

where $\Delta\varepsilon$ is the change in applied strain. The strain sensitivity of the thin film was equivalent to and obtained from the slope of the linear least-squares regression line fitted to each dataset shown in Fig. 8. Similar to Section 4.1, CNT density was also varied (N = 1,400, 1,800, and 2,400), and the strain sensitivity

results are summarized in Fig. 9. Each data point corresponds to the average of 20 strain sensitivity simulations. A general trend was that, as the number of CNTs increased, strain sensitivity decreased, which was consistent with previous works and other experimental and numerical studies [11, 16]. In particular, it can be seen in Fig. 9 that Model #1 with straight CNTs exhibited the highest strain sensitivities among the cases investigated. Model #2 and Model #5 showed similar strain sensitivities. For example, when N = 2,400, the average strain sensitivities of Model #2 and Model #5 were 0.923 and 0.925, respectively. On the other hand, strain sensitivities of Model #3 were the smallest of the five. These results suggest that a highly simplified CNT-based thin film model assuming that all CNTs are straight would tend to overestimate strain sensitivity (*i.e.*, within the framework of the assumptions presented in this numerical simulations study). Nevertheless, a more general conclusion is that the geometric shapes of CNTs is an important parameter that governs bulk film electrical and electromechanical properties and should be considered.

4.3 Experimental validation

To validate the 2D CNT-based thin film model, MWCNT-PSS thin films were fabricated using a vacuum filtration method [10]. First, 0.75 mg/mL MWCNT-PSS solution was prepared following the procedures mentioned in section 2.2. The solution was then vacuum-filtered using a polytetrafluoroethylene membrane filter. Upon filtration and air-drying, the thin film was cut to form smaller (~4×33 mm^2) specimens. Then, two single-strand wires were affixed at opposite ends of the film, using silver paste, to form the electrodes. After drying the silver paste for ~4 h in air, the nominal electrical resistance of the specimen was measured using a Keysight 34461A digital multimeter.

It should be mentioned that the films tested in these experiments were different than those used for AFM characterization (section 2.2). In these experiments, MWCNT-PSS thin films were electrically percolated (*i.e.*, conductive) and were characterized by an average nominal (unstrained) resistance of 42.98 Ω. The objective here was to study their bulk film electrical properties, as opposed to trying to identify individual nanotube physical properties. Then, the films were mounted in a Test Resources 150R load frame and subjected to monotonic uniaxial tensile tests. Tensile strains up to 2,500 με were applied at a load rate of 5,000 με/min. Fig. 10 shows a representative result in which the normalized change in resistance of the thin film is plotted as a function of applied strains. It can be observed that, similar to the 2D numerical modeling results (Fig. 8), the experiments revealed that MWCNT-PSS thin films also exhibited linear strain sensing properties.

5 Conclusions

In this study, 2D percolation-based numerical models of CNT-based thin films were derived using AFM measurements of the physical properties of as-deposited MWCNTs. First, ultra-low-concentration MWCNT-PSS thin films were assembled by drying dispersed solutions on silicon substrates. Second, AFM images of these MWCNT-PSS thin films were obtained. The AFM images were processed to estimate the lengths of individual MWCNTs. It was found that the average length of 20 MWCNTs was 1.904 μm, which was shorter than their initial state (3 μm), suggesting that nanotubes were cut during dispersion. Moreover, the image analysis results demonstrated that dispersed MWCNTs, when deposited, could be characterized by complex geometric shapes, and three dominant shapes were identified for numerical modeling purposes.

The image analysis results were incorporated in 2D CNT-based nanocomposite models. First, all of the models were generated considering that CNTs could possess different lengths, and its statistical distribution followed those found in experiments (*i.e.*, from image analysis). To incorporate the three different CNT shapes in the model, these shapes were assumed to be composed of equidistant linear segments connected at the nodes, and the angle at each node was randomly generated. The model also randomly deposited CNTs in a 10×60 μm^2 representative area, but the number or density of CNTs was predefined. Using this model, its electrical resistance was estimated using Kirchhoff's current law and the conductance version of Ohm's. Then, the simulations considered applying uniaxial tensile-compressive strains to the percolation-based model so as to investigate how the bulk film properties would change in response to applied strains.

This work considered five different models to explore the effects of CNT morphology on bulk film electrical and electromechanical properties. It was found that the unstrained electrical resistance of models that incorporated more complex geometric shapes of CNTs were higher than a simplified case with only straight CNTs. In particular, given the same CNT density, electrical resistance was sensitive to effective CNT length. In addition, the morphology of the CNT network also affected the film's electromechanical behavior. The results showed that the CNT network with straight CNTs was more sensitive to mechanical strains as compared to other thin film models. The thin film model that included CNTs with three linear segments exhibited the lowest strain sensitivity among

the five different thin film models. Overall, these results suggest that the geometric shapes of CNTs can contribute significantly to affect bulk film electrical and electromechanical properties.

Acknowledgments

This research was supported by the U.S. National Science Foundation (NSF) Faculty Early Career Development (CAREER) Program under grant number CMMI-1253564. Additional support was provided by the Jacobs School of Engineering, University of California-San Diego.

References

1. Farrar CR, Worden K (2007) An introduction to structural health monitoring. Phil. Trans. R. Soc. A, London, UK
2. Knite M, Teteris V, Kiploka A, Kaupuzs J (2004) Polyisoprene-carbon black nanocomposites as tensile strain and pressure sensor materials. Sens Actuators A: Phys 110: 142-149 doi: 10.1016/j.sna.2003.08.006
3. Loh KJ, Kim J, Lynch JP, Kam NWS, Kotov NA (2007) Multifunctional layer-by-layer carbon nanotube–polyelectrolyte thin films for strain and corrosion sensing. Smart Mater Struct 16: 429 doi: 10.1088/0964-1726/16/2/022
4. Bae S-H, Lee Y, Sharma BK, Lee H-J, Kim J-H, Ahn J-H (2013) Graphene-based transparent strain sensor. Carbon 51: 236-242 doi: http://dx.doi.org/10.1016/j.carbon.2012.08.048
5. Lee J, Kim S, Lee J, Yang D, Park BC, Ryu S, Park I (2014) A stretchable strain sensor based on a metal nanoparticle thin film for human motion detection. Nanoscale 6: 11932-11939 doi: 10.1039/C4NR03295K
6. Maia F, Tedim J, Bastos AC, Ferreira MGS, Zheludkevich ML (2013) Nanocontainer-based corrosion sensing coating. Nanotechnology 24: 415502 doi: 10.1088/0957-4484/24/41/415502
7. Iijima S (1991) Helical microtubules of graphitic carbon. Nature 354: 56-58 doi: 10.1038/354056a0
8. Baughman RH, Zakhidov AA, de Heer WA (2002) Carbon nanotubes--the route toward applications. Science 297: 787-792 doi: 10.1126/science.1060928
9. Stampfer C, Jungen A, Linderman R, Obergfell D, Roth S, Hierold C (2006) Nano-electromechanical displacement sensing based on single-walled carbon nanotubes. Nano Lett 6: 1449-1453 doi: 10.1021/nl0606527
10. Dharap P, Li Z, Nagarajaiah S, Barrera EV (2004) Nanotube film based on single-wall carbon nanotubes for strain sensing. Nanotechnology 15: 379-382 doi: 10.1088/0957-4484/15/3/026
11. Pham GT, Park Y-B, Liang Z, Zhang C, Wang B (2008) Processing and modeling of conductive thermoplastic/carbon nanotube films for strain sensing. Composites Part B 39: 209-216 doi: 10.1016/j.compositesb.2007.02.024
12. Loyola BR, Zhao Y, Loh KJ, La Saponara V (2013) The electrical response of carbon nanotube-based thin film sensors subjected to mechanical and environmental effects. Smart Mater Struct 22: 025010 doi: 10.1088/0964-1726/22/2/025010
13. Gupta S, Gonzalez JG, Loh KJ (2016) Self-sensing concrete enabled by nano-engineered cement–aggregate interfaces. Struct Health Monit: 1475921716643867 doi: 10.1177/1475921716643867
14. Behnam A, Ural A (2007) Computational study of geometry-dependent resistivity scaling in single-walled carbon nanotube films. Phys Rev B 75: 125432 doi: 10.1103/PhysRevB.75.125432
15. Bao WS, Meguid SA, Zhu ZH, Weng GJ (2012) Tunneling resistance and its effect on the electrical conductivity of carbon nanotube nanocomposites. J Appl Phys 111: 093726 doi: 10.1063/1.4716010
16. Hu N, Karube Y, Yan C, Masuda Z, Fukunaga H (2008) Tunneling effect in a polymer/carbon nanotube nanocomposite strain sensor. Acta Mater 56: 2929-2936 doi: 10.1016/j.actamat.2008.02.030
17. Rahman R, Servati P (2012) Effects of inter-tube distance and alignment on tunnelling resistance and strain sensitivity of nanotube/polymer composite films. Nanotechnology 23: 055703 doi: 10.1088/0957-4484/23/5/055703
18. Lee BM, Loh KJ (2015) A 2D percolation-based model for characterizing the piezoresistivity of carbon nanotube-based films. J Mater Sci 50: 2973-2983 doi: 10.1007/s10853-015-8862-y
19. Hu N, Karube Y, Arai M, Watanabe T, Yan C, Li Y, Liu Y, Fukunaga H (2010) Investigation on sensitivity of a polymer/carbon nanotube composite strain sensor. Carbon 48: 680-687 doi: 10.1016/j.carbon.2009.10.012
20. Lee BM, Wang L, Loh KJ (2015) Characterization of carbon nanotube strain sensors using experimental tests and percolation modeling. In: Structural Health Monitoring 2015, Stanford, CA, September 2015. DEStech Publications, Inc. doi:10.12783/SHM2015/271
21. Amini A, Bahreyni B (2012) Behavioral model for electrical response and strain sensitivity of nanotube-based nanocomposite materials. J Vac Sci Technol, B 30: 022001 doi: 10.1116/1.3691654
22. Yin G, Hu N, Karube Y, Liu Y, Li Y, Fukunaga H (2011) A carbon nanotube/polymer strain sensor with linear and anti-symmetric piezoresistivity. J Compos Mater 45: 1315-1323 doi: 10.1177/0021998310393296

23. Gommes C, Blacher S, Masenelli-Varlot K, Bossuot C, McRae E, Fonseca A, Nagy JB, Pirard JP (2003) Image analysis characterization of multi-walled carbon nanotubes. Carbon 41: 2561-2572 doi: 10.1016/S0008-6223(03)00375-0
24. Tenent RC, Barnes TM, Bergeson JD, Ferguson AJ, To B, Gedvilas LM, Heben MJ, Blackburn JL (2009) Ultrasmooth, large-area, high-uniformity, conductive transparent single-walled-carbon-nanotube films for photovoltaics produced by ultrasonic spraying. Adv Mater 21: 3210-3216 doi: 10.1002/adma.200803551
25. Timmermans MY, Estrada D, Nasibulin AG, Wood JD, Behnam A, Sun D-m, Ohno Y, Lyding JW, Hassanien A, Pop E, Kauppinen EI (2012) Effect of carbon nanotube network morphology on thin film transistor performance. Nano Res 5: 307-319 doi: 10.1007/s12274-012-0211-8
26. McEuen PL, Park J-Y (2004) Electron transport in single-walled carbon nanotubes. MRS Bulletin 29: 272-275 doi: doi:10.1557/mrs2004.79
27. Baughman RH, Zakhidov AA, de Heer WA (2002) Carbon nanotubes-the route toward applications. Science 297: 787-792 doi: 10.1126/science.1060928
28. Fuhrer MS, Lim AKL, Shih L, Varadarajan U, Zettl A, McEuen PL (2000) Transport through crossed nanotubes. Physica E 6: 868-871 doi: 10.1016/S1386-9477(99)00228-3
29. Bandaru PR (2007) Electrical properties and applications of carbon nanotube structures. J Nanosci Nanotechnol 7: 1239-1267 doi: 10.1166/jnn.2007.307
30. Wang L, Loh KJ, Brely L, Bosia F, Pugno NM (2016) An experimental and numerical study on the mechanical properties of carbon nanotube-latex thin films. J Eur Ceram Soc 36: 2255-2262 doi: 10.1016/j.jeurceramsoc.2015.12.052
31. Cao J, Wang Q, Dai H (2003) Electromechanical properties of metallic, quasimetallic, and semiconducting carbon nanotubes under stretching. Phys Rev Lett 90: 157601 doi:
32. Zeng X, Xu X, Shenai PM, Kovalev E, Baudot C, Mathews N, Zhao Y (2011) Characteristics of the electrical percolation in carbon nanotubes/polymer nanocomposites. J Phys Chem C 115: 21685-21690 doi: 10.1021/jp207388n
33. Li C, Thostenson ET, Chou T-W (2008) Effect of nanotube waviness on the electrical conductivity of carbon nanotube-based composites. Compos Sci Technol 68: 1445-1452 doi: 10.1016/j.compscitech.2007.10.056
34. Li C, Chou T-W (2007) Continuum percolation of nanocomposites with fillers of arbitrary shapes. Appl Phys Lett 90: 174108 doi: 10.1063/1.2732201

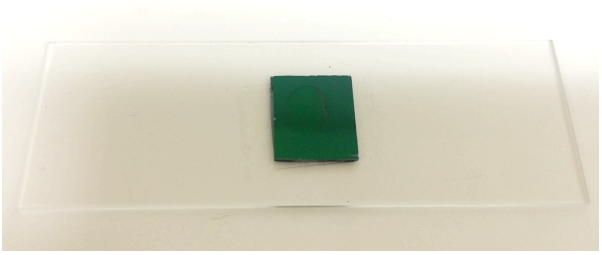

Fig. 1 A small drop of 1 μg/ml MWCNT-PSS solution was pipetted onto a silicon substrate (~7×7 mm^2) and air-dried for AFM imaging.

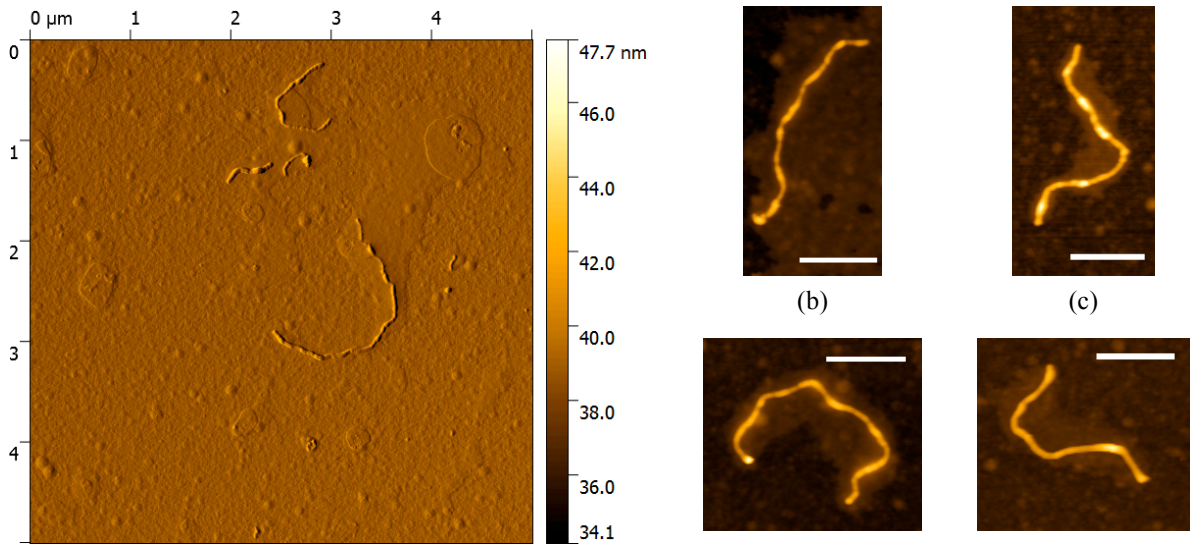

Fig. 2 (a) The AFM amplitude image describes the surface topography of the MWCNT-PSS thin film. (b)-(e) AFM height images show various geometrical shapes of as-deposited MWCNTs. All scale bars represent 500 nm.

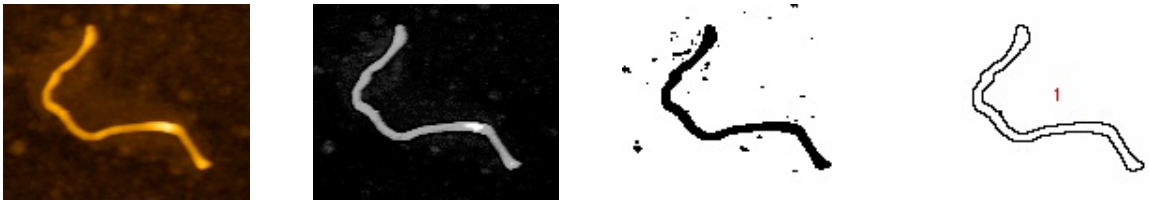

(a) (b) (c) (d)

Fig. 3 The length of an MWCNT was estimated following four steps: (a) select the region of interest in the AFM image (RGB image); (b) convert the RGB image into a gray-scale image; (c) convert gray-scale image into a binary image; and (d) measure the perimeter or length of the MWCNT.

Table 1 An MWCNT's length was measured using two methods and compared

	Linear segment method (*MATLAB*)		Perimeter method (I*mageJ*)
	Number of segments	Estimated length (μm)	Estimated length (μm)
MWCNT 1	7	1.488	1.623
	14	1.590	
MWCNT 2	15	2.557	2.734
	20	2.581	

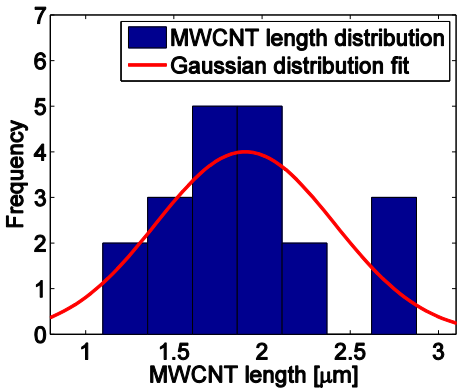

Fig. 4 The histogram plots the distribution of different CNT lengths measured, and a Gaussian distribution was fitted to the raw data to obtain its average length of 1.904 μm and standard deviation of 0.506 μm.

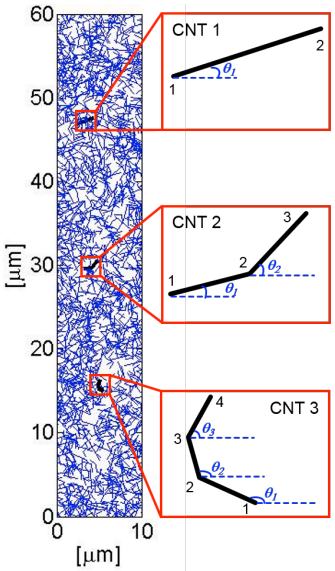

Fig. 5 A representative 2D CNT-based thin film model (N = 1,400) was generated by randomly dispersing three types of CNTs (CNT 1, 2, and 3) within a 10×60 μm^2 area.

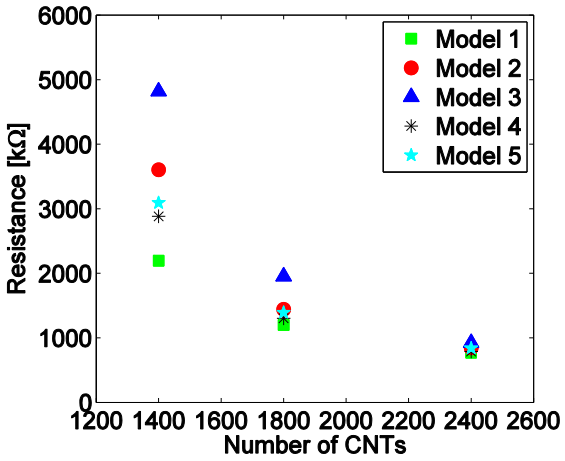

Fig. 6 The average nominal (or unstrained) electrical resistances of five different CNT-based thin film models were simulated along with different CNT densities (N = 1,400, 1,800, and 2,400).

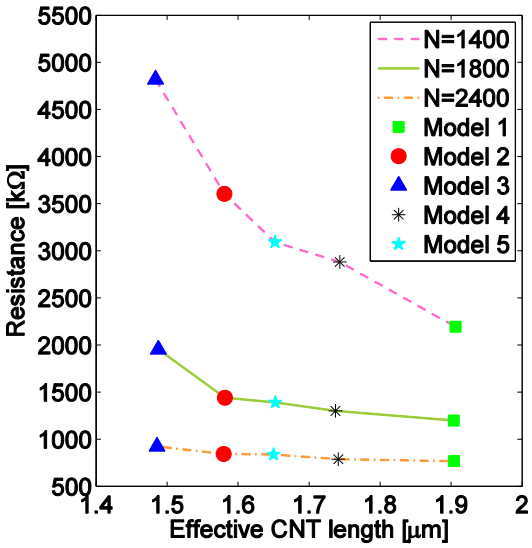

Fig. 7 The unstrained resistances of different thin film models were plotted as a function of effective CNT lengths. Three different CNT densities (N = 1,400, 1,800, and 2,400) were considered.

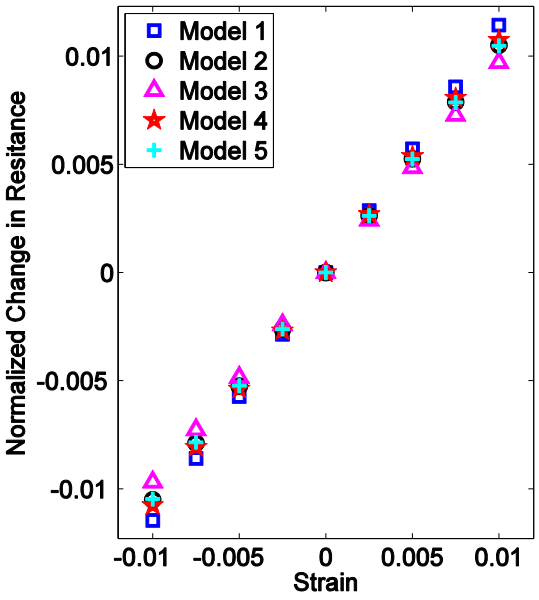

Fig. 8 The normalized change in resistance was plotted as a function of applied strain. All five different types of CNT-based thin film models exhibited linear piezoresistivity.

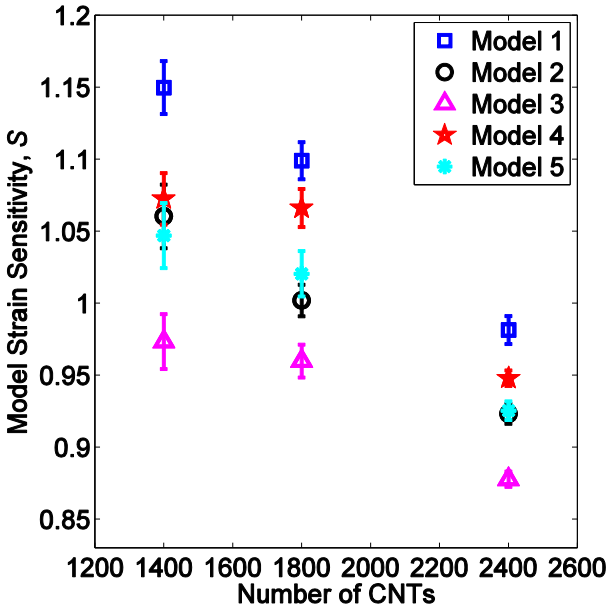

Fig. 9 Strain sensitivities of 10×60 μm^2 CNT-based thin film models (with standard error of the mean plotted as error bars) were evaluated as a function of CNT density or *N*.

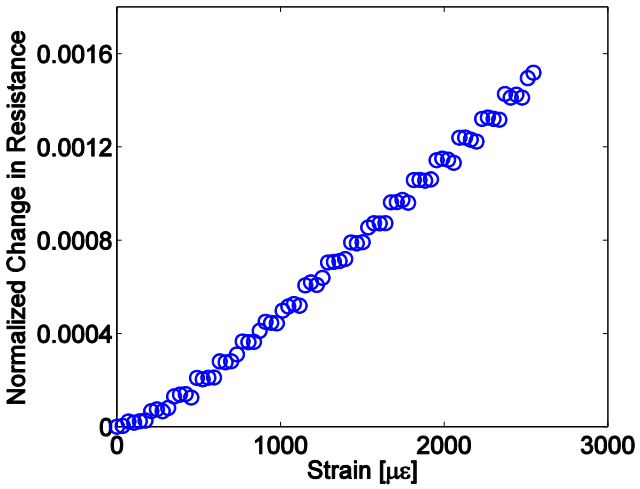

Fig. 10 A 0.75 mg/mL MWCNT-PSS thin film was subjected to uniaxial tensile strains to 2,500 με.